Engineering Analysis with Boundary Elements 34 (2010) 377–387

Contents lists available at ScienceDirect

Engineering Analysis with Boundary Elements

journal homepage: www.elsevier.com/locate/enganabound

A 2D time-domain collocation-Galerkin BEM for dynamic crack analysis in piezoelectric solids

M. Wünsche [a,c], F. García-Sánchez [b,*], A. Sáez [a], Ch. Zhang [c]

[a] Departamento de Mecánica de Medios Continuos, Universidad de Sevilla, Camino de los Descubrimientos s/n, 41092 Sevilla, Spain
[b] Departamento de Ingeniería Civil, de Materiales y Fabricación, E.T.S. de Ingenieros Industriales, Universidad de Málaga, Campus de El Ejido s/n, 29013 Málaga, Spain
[c] Department of Civil Engineering, University of Siegen, D-57068 Siegen, Germany

ARTICLE INFO

Article history:
Received 18 June 2009
Accepted 26 November 2009
Available online 23 December 2009

Keywords:
Time-domain BEM
Galerkin-method
Dynamic crack analysis
Piezoelectric solids
Dynamic intensity factors

ABSTRACT

A time-domain boundary element method (TDBEM) for transient dynamic analysis of two-dimensional (2D), homogeneous, anisotropic and linear piezoelectric cracked solids is presented in this paper. The present analysis uses a combination of the strongly singular displacement boundary integral equations (BIEs) and the hypersingular traction boundary integral equations. The spatial discretization is performed by a Galerkin-method, while a collocation method is implemented for the temporal discretization. Both temporal and spatial integrations are carried out analytically. In this way, only the line integrals over a unit circle arising in the time-domain fundamental solutions are computed numerically by standard Gaussian quadrature. An explicit time-stepping scheme is developed to compute the unknown boundary data including the generalized crack-opening-displacements (CODs) numerically. Special crack-tip elements are adopted to ensure a direct and an accurate computation of the dynamic field intensity factors (IFs) from the CODs. Several numerical examples involving stationary cracks in both infinite and finite solids under impact loading are presented to show the accuracy and the efficiency of the developed hypersingular time-domain BEM.

1. Introduction

Piezoelectric materials are widely applied in smart devices and structures like transducers, actuators and sensors due to their inherent coupling effects between mechanical and electrical fields. Dynamic crack analysis in piezoelectric solids is of considerable importance in the fields of fracture and damage mechanics, design and optimization as well as non-destructive material testing of piezoelectric structures [22]. Analytical solutions are available only for very simple crack geometries and loading conditions, so that numerical methods are needed to solve more general problems. Several numerical methods have been developed to solve the resulting initial-boundary value problems for 2D dynamic crack analysis in piezoelectric solids. The finite element method (FEM) has been applied by Enderlein et al. [9,10]. Meshless approaches have been successfully applied by Liu et al. [23] for time-harmonic problems and Sladek et al. [31–33] for transient problems. An attractive method for the solution of dynamic crack problems in piezoelectric solids is the boundary element method (BEM). Although the boundary element method has been successfully applied to dynamic crack analysis in homogeneous, isotropic and linear elastic solids since many years (e.g., [1,8]), its extension and applications to generally anisotropic and piezoelectric materials is not straight-forward, because the required dynamic fundamental solutions do not have closed-form expressions and are mathematically complex, which affects an easy and efficient numerical implementation. Dynamic fundamental solutions for piezoelectric materials in the frequency-domain and the time-domain have been presented by Daros et al. [4,5], Denda et al. [6], Khutoryansky and Sosa [20,21], Norris [26] and Wang et al. [35]. To circumvent this difficulty, dual reciprocity BEM formulations based on the corresponding static fundamental solutions have been developed by Dziatkiewicz and Fedelinski [7] and Kögl and Gaul [19]. However, in this method interior nodes are necessary to describe the inertial effects accurately and the radiation conditions at infinity are not automatically satisfied.

Two-dimensional frequency-domain BEM using time-harmonic dynamic fundamental solution have been presented by Denda et al. [6] for eigenvalue analysis, and by Gross et al. [15] and Sáez et al. [28] for time-harmonic crack analysis. A time-domain BEM for transient dynamic analysis of a cracked piezoelectric solid has been presented by García-Sánchez et al. [11,13]. In these works the convolution quadrature formula of Lubich [24,25] has been adopted for the temporal discretization, which requires the Laplace-domain instead of the time-domain fundamental solutions, while a collocation method has been implemented for the

* Corresponding author.
E-mail addresses: wuensche@bauwesen.uni-siegen.de (M. Wünsche), fgsanchez@uma.es (F. García-Sánchez), andres@us.es (A. Sáez), c.zhang@uni-siegen.de (Ch. Zhang).

0955-7997/$ - see front matter © 2009 Elsevier Ltd. All rights reserved.
doi:10.1016/j.enganabound.2009.11.004

spatial discretization. A comparative study of the time-domain BEM using the convolution quadrature formula of Lubich, frequency-domain and Laplace-domain BEM for transient dynamic crack analysis in anisotropic solids can be found in García-Sánchez et al. [12]. Meanwhile, a comparative study of the classical time-domain BEM and the time-domain BEM using the convolution quadrature formula of Lubich for transient dynamic crack analysis in anisotropic solids has been recently presented by Wünsche et al. [36], where the spatial discretization is performed by a Galerkin-method in both variants.

In this paper a dual time-domain boundary element method (TDBEM) [17,18] for transient dynamic crack analysis in two-dimensional (2D), homogeneous, anisotropic and linear piezoelectric solids is presented. Both infinite and finite cracked solids subjected to impact loading are considered. A combination of the classical displacement boundary integral equations (BIEs) and the hypersingular traction BIEs is applied in the TDBEM to solve the initial-boundary value problem. In contrast to [17] where traction and displacement BIEs are used over crack-faces, in this work only traction BIEs are used over the crack-faces while the displacement BIEs are used only over external boundaries. The spatial discretization is performed by a Galerkin-method while a collocation method is adopted for the temporal discretization. The time-domain dynamic fundamental solutions derived by Wang and Zhang [35] are implemented. For the spatial discretization of the boundary values, two different shape functions are applied. On the external boundary and on the crack-faces away from the crack-tips, standard linear elements are adopted, while special crack-tip elements are introduced at the crack-tips to describe the local square-root behavior of the generalized crack-opening-displacements (CODs) properly. Analytical techniques are used in the present time-domain BEM to directly compute the strongly singular and hypersingular boundary integrals without regularization. By using linear temporal shape functions, the time integrations can also be carried out analytically. Subsequently, only the line integrals over the unit circle arising in the time-domain fundamental solutions need to be computed numerically by standard Gaussian quadratures. An explicit time-stepping scheme is developed to compute the unknown boundary data. To demonstrate the accuracy and the efficiency of the present TDBEM, numerical results for the dynamic field intensity factors (IFs: stress and electric displacement intensity factors) are presented and compared with the results obtained by the finite element method and other BEM formulations.

As compared with previous BEM approaches, the present formulation is computationally faster than the ones based on working either in the frequency or Laplace domains and subsequently applying the FFT or inverse Laplace transform [12,28]. It is applicable to both finite and infinite piezoelectric solids and there is no need to define internal nodes in the domain, as compared to the dual reciprocity BEM approaches previously mentioned [7,19].

With respect to the formulations based on direct integration in the time domain, they are generally faster but the spatial and temporal discretizations must fulfill certain limitations in order to maintain the stability of the result [8]. Such limitations are less restrictive in the case of the present collocation-Galerkin BEM [36], in such way that computational costs become comparable. Besides, if the dual BEM is considered to circumvent the degeneration of the crack problem, computation of the hypersingular integrals arising in the formulation [11–13] is less involved in the case of the collocation-Galerkin BEM, since the strength of such hypersingular kernels is equivalent to the Cauchy principal value integrals in the collocation method [14,3], so that standard continuous elements may be used for the spatial discretization of the crack-faces.

Formulations based on Lubich's quadratures to compute the convolution integrals in the time domain BEM [11,13] are extremely stable and the spatial and temporal discretizations are rather independent. However, their computational cost is much larger than in the present collocation-Galerkin BEM [36].

2. Problem statement and time-domain BIEs

Let Ω be a homogeneous, anisotropic and linear piezoelectric solid with boundary Γ that contains a crack of arbitrary shape, as shown in Fig. 1. In the absence of body forces and electrical charges, using the quasi-electrostatic assumption and the generalized notation introduced by Barnett and Lothe [2], the equations of motion and the constitutive relations can be written as

$$\sigma_{ij,i}(\mathbf{x},t)=\rho\delta^*_{JK}\ddot{u}_K(\mathbf{x},t), \tag{1}$$

$$\sigma_{ij}(\mathbf{x},t)=C_{ijKl}u_{K,l}(\mathbf{x},t), \tag{2}$$

where ρ is the mass density and the generalized displacements u_I, the generalized stresses σ_{ij}, and generalized elastic matrix C_{iJKl}; containing mechanical and electrical variables, are defined as following:

$$u_I=\begin{cases} u_i, & I=1,2,\ \text{displacements},\\ \phi, & I=4\ \text{electricpotential},\end{cases} \tag{3}$$

$$\sigma_{ij}=\begin{cases} \sigma_{ij}, & J=1,2,\ \text{stresses},\\ D_i, & J=4\ \text{electric displacements},\end{cases} \tag{4}$$

$$C_{iJKl}=\begin{cases} c_{ijkl}, & J,K=1,2,\ \text{elasticity tensor},\\ e_{lij}, & J=1,2;\ K=4,\ \text{piezoelectric tensor},\\ e_{ikl}, & J=4;\ K=1,2,\\ -\varepsilon_{il}, & J=K=4\ \text{permitivity tensor}.\end{cases} \tag{5}$$

and the generalized Kronecker delta δ^*_{JK} is defined by

$$\delta^*_{JK}=\begin{cases}\delta_{jk}, & J,K=1,2,\\ 0 & \text{otherwise}.\end{cases} \tag{6}$$

By virtue of the symmetry of elasticity, piezoelectric and permittivity tensors, the generalized elasticity tensor satisfies the following symmetry condition

$$C_{iJKl}=C_{lKJi}. \tag{7}$$

Throughout the analysis, a comma after a quantity designates spatial derivatives, while superscript dots stand for temporal derivatives of the quantity. Lower case Latin indices take the values 1 and 2 (elastic), while capital Latin indices take the values 1, 2 (elastic) and 4 (electric). Unless otherwise stated, the conventional summation rule over repeated indices is implied.

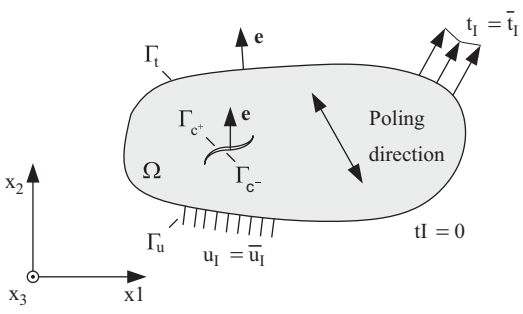

Fig. 1. A cracked piezoelectric solid.

The cracked solid Ω satisfies the initial conditions at $t=0$

$$u_I(\mathbf{x}, t=0)=0; \quad \dot{u}_I(\mathbf{x}, t=0)=0, \tag{8}$$

the boundary conditions on the external boundary $\Gamma_b=\Gamma_u \bigcup \Gamma_t$

$$u_I(\mathbf{x}, t)=\overline{u}_I(\mathbf{x}, t), \quad \mathbf{x}\in\Gamma_u, \tag{9}$$

$$t_I(\mathbf{x}, t)=\overline{t}_I(\mathbf{x}, t), \quad \mathbf{x}\in\Gamma_t, \tag{10}$$

with t_I being the generalized tractions vector

$$t_I(\mathbf{x}, t)=\sigma_{jI}(\mathbf{x}, t)e_j(\mathbf{x}), \tag{11}$$

where e_j denotes the outward unit normal to the boundary, Γ_t represents the external boundary where the generalized tractions t_I are given and Γ_u is the external boundary where the generalized displacements u_I are prescribed. On the crack-faces $\Gamma_c=\Gamma_{c^+}\bigcup\Gamma_{c^-}$, with Γ_{c^+} and Γ_{c^-} denoting the upper and the lower crack-face (Fig. 1), null or self-equilibrated mechanical tractions are considered, while two different electric boundary conditions are applied:

- Impermeable crack: the electric crack-face boundary conditions are given by

$$D_i(\mathbf{x}\in\Gamma_{c^+}, t)=D_i(\mathbf{x}\in\Gamma_{c^-}, t)=0. \tag{12}$$

- Permeable crack: the electric crack-face boundary conditions are given in such case by

$$D_i(\mathbf{x}\in\Gamma_{c^+}, t)=D_i(\mathbf{x}\in\Gamma_{c^-}, t), \quad \phi(\mathbf{x}\in\Gamma_{c^+}, t)=\phi(\mathbf{x}\in\Gamma_{c^-}, t). \tag{13}$$

In this paper the problem is addressed by a dual BEM formulation [13,17], so that the time-domain displacement BIEs for a cracked solid are applied on the external boundary Γ_b

$$c_{IJ}u_I(\mathbf{x}, t)=\int_{\Gamma_b}[u^G_{IJ}(\mathbf{x}, \mathbf{y}, t)*t_I(\mathbf{y}, t)-t^G_{IJ}(\mathbf{x}, \mathbf{y}, t) *u_I(\mathbf{y}, t)]\,\mathrm{d}\Gamma_y+\int_{\Gamma_{c^+}} t^G_{IJ}(\mathbf{x}, \mathbf{y}, t)*\Delta u_I(\mathbf{y}, t)\,\mathrm{d}\Gamma_y, \mathbf{x}\in\Gamma_b. \tag{14}$$

In Eq. (14) $u^G_{IJ}(\mathbf{x}, \mathbf{y}, t)$ and $t^G_{IJ}(\mathbf{x}, \mathbf{y}, t)$ are, respectively, time domain displacement and traction fundamental solutions, c_{IJ} is the free term, the asterisk " $*$ " denotes the Riemann convolution, and $\Delta u_I(\mathbf{x}, t)$ are the generalized crack-opening-displacements (CODs) defined by

$$\Delta u_I(\mathbf{x}, t)=u_I(\mathbf{x}\in\Gamma_{c^+}, t)-u_I(\mathbf{x}\in\Gamma_{c^-}, t), \quad \mathbf{x}\in\Gamma_c. \tag{15}$$

The traction fundamental solutions $t^G_{IJ}(\mathbf{x}, \mathbf{y}, t)$ are obtained by substitution of the displacement fundamental solutions into (2) and (11) to yield

$$t^G_{IJ}(\mathbf{x}, \mathbf{y}, t)=C_{qIKr}e_q(\mathbf{y})u^G_{KJ,r}(\mathbf{x}, \mathbf{y}, t). \tag{16}$$

The time-domain traction BIEs are obtained by substituting Eq. (14) into Eqs. (2) and (11). Taking into account the boundary conditions the resulting BIEs can be applied on either of the crack-faces (say Γ_{c^+}) to yield a complete set of independent [13,17] for the displacements and the tractions on Γ_b and the CODs on Γ_c

$$t_J(\mathbf{x}, t)=\int_{\Gamma_b}[v^G_{IJ}(\mathbf{x}, \mathbf{y}, t)*t_I(\mathbf{y}, t)-w^G_{IJ}(\mathbf{x}, \mathbf{y}, t) *u_I(\mathbf{y}, t)]\,\mathrm{d}\Gamma_y+\int_{\Gamma_{c^+}} w^G_{IJ}(\mathbf{x}, \mathbf{y}, t)*\Delta u_I(\mathbf{y}, t)\,\mathrm{d}\Gamma_y, \mathbf{x}\in\Gamma_{c^+}, \tag{17}$$

where $v^G_{IJ}(\mathbf{x}, \mathbf{y}, t)$ and $w^G_{IJ}(\mathbf{x}, \mathbf{y}, t)$ are the traction and the higher-order traction fundamental solutions, which are defined by

$$v^G_{IJ}(\mathbf{x}, \mathbf{y}, t)=-C_{pIKs}e_p(\mathbf{x})u^G_{KJ,s}(\mathbf{x}, \mathbf{y}, t), \tag{18}$$

$$w^G_{IJ}(\mathbf{x}, \mathbf{y}, t)=-C_{pIKs}e_p(\mathbf{x})C_{qJLr}e_q(\mathbf{y})u^G_{KL,sr}(\mathbf{x}, \mathbf{y}, t). \tag{19}$$

The displacement BIEs (14) are strongly singular, while the tractions BIEs (17) show a hypersingular behavior as $\mathbf{x}\to\mathbf{y}$.

Furthermore, in this work a spatial Galerkin-method is implemented, so that the time-domain BIEs (14) and (17) are treated in a weighted residual sense [30,36], to yield

$$\int_{\Gamma_b}\psi(\mathbf{x})u_J(\mathbf{x}, t)\,\mathrm{d}\Gamma_x=\int_{\Gamma_b}\psi(\mathbf{x})\int_{\Gamma_b}[u^G_{IJ}(\mathbf{x}, \mathbf{y}, t)*t_I(\mathbf{y}, t)-t^G_{IJ}(\mathbf{x}, \mathbf{y}, t) *u_I(\mathbf{y}, t)]\,\mathrm{d}\Gamma_y\,\mathrm{d}\Gamma_x+\int_{\Gamma_b}\psi(\mathbf{x})\int_{\Gamma_{c^+}} t^G_{IJ}(\mathbf{x}, \mathbf{y}, t) *\Delta u_I(\mathbf{y}, t)\,\mathrm{d}\Gamma_y\,\mathrm{d}\Gamma_x, \tag{20}$$

$$\int_{\Gamma_{c^+}}\psi(\mathbf{x})t_J(\mathbf{x}, t)\,\mathrm{d}\Gamma_x=\int_{\Gamma_{c^+}}\psi(\mathbf{x})\int_{\Gamma_b}[v^G_{IJ}(\mathbf{x}, \mathbf{y}, t) *t_I(\mathbf{y}, t)-w^G_{IJ}(\mathbf{x}, \mathbf{y}, t) *u_I(\mathbf{y}, t)]\,\mathrm{d}\Gamma_y\,\mathrm{d}\Gamma_x+\int_{\Gamma_{c^+}}\psi(\mathbf{x})\int_{\Gamma_{c^+}} w^G_{IJ}(\mathbf{x}, \mathbf{y}, t) *\Delta u_I(\mathbf{y}, t)\,\mathrm{d}\Gamma_y\,\mathrm{d}\Gamma_x, \tag{21}$$

where $\psi(\mathbf{x})$ is the test or weight function. Here, $\psi(\mathbf{x})$ is chosen to coincide with the spatial shape function employed for the interpolation of the boundary values.

3. Time-domain dynamic fundamental solutions

The time-domain dynamic fundamental solutions for homogeneous, anisotropic and linear piezoelectric solids are not available in explicit form. Here, the solutions derived by Wang and Zhang [35] using the Radon transform technique are implemented. Such solutions are expressed in the 2D case by a line integral over the unit circle as

$$u^G_{IJ}(\mathbf{x}, \mathbf{y}, t)=\frac{\mathrm{H}(t)}{4\pi^2}\int_{|\mathbf{n}|=1}\sum_{m=1}^{3}\frac{P^m_{IJ}}{\rho c_m}\frac{1}{c_m t+\mathbf{n}(\mathbf{y}-\mathbf{x})}\,\mathrm{d}\mathbf{n}, \tag{22}$$

where $\mathrm{H}(t)$, c_m and $P^m_{IJ}(\mathbf{n})$ denote, respectively, the Heaviside step function, the phase velocities of the elastic waves and the projection operator (see Appendix A.1 for details).

Integrating Eq. (22) by parts with respect to the time and applying the properties of convolution integrals, the time-domain displacement fundamental solutions can be split into a singular (static) part plus a regular (dynamic) part as

$$u^G_{IJ}(\mathbf{x}, \mathbf{y}, t)*f(t)=u^S_{IJ}(\mathbf{x}, \mathbf{y})f(t)+u^R_{IJ}(\mathbf{x}, \mathbf{y}, t)*\dot{f}(t), \tag{23}$$

where the superscripts S and R stand for static (singular) and dynamic (regular) parts, respectively.

Similarly, the traction and the higher-order traction fundamental solutions can also be divided into their singular static and regular dynamic parts as

$$t^G_{IJ}(\mathbf{x}, \mathbf{y}, t)*f(t)=t^S_{IJ}(\mathbf{x}, \mathbf{y})f(t)+t^R_{IJ}(\mathbf{x}, \mathbf{y}, t)*\ddot{f}(t), \tag{24}$$

$$v^G_{IJ}(\mathbf{x}, \mathbf{y}, t)*f(t)=v^S_{IJ}(\mathbf{x}, \mathbf{y})f(t)+v^R_{IJ}(\mathbf{x}, \mathbf{y}, t)*\ddot{f}(t), \tag{25}$$

$$w^G_{IJ}(\mathbf{x}, \mathbf{y}, t)*f(t)=w^S_{IJ}(\mathbf{x}, \mathbf{y})f(t)+w^R_{IJ}(\mathbf{x}, \mathbf{y}, t)*\ddot{f}(t). \tag{26}$$

The dynamic and static parts of the time-domain fundamental solutions can be found, respectively, in Appendices A.1 and A.2.

In addition, the time-domain fundamental solutions possess the following spatial symmetry properties

$$u^G_{IJ}(\mathbf{x}, \mathbf{y}, t)=u^G_{JI}(\mathbf{y}, \mathbf{x}, t), \tag{27}$$

$$t^G_{IJ}(\mathbf{x}, \mathbf{y}, t)=-v^G_{IJ}(\mathbf{x}, \mathbf{y}, t)=v^G_{JI}(\mathbf{y}, \mathbf{x}, t), \tag{28}$$

$$w^G_{IJ}(\mathbf{x}, \mathbf{y}, t)=w^G_{JI}(\mathbf{y}, \mathbf{x}, t). \tag{29}$$

4. Numerical solution procedure

A numerical solution procedure is developed in this section to solve the time-domain BIEs (20) and (21). The procedure uses a Galerkin-method for the spatial discretization and a collocation method for the temporal discretization. In the following, some details of the numerical solution algorithm are described.

4.1. Spatial and temporal discretizations

The external boundary Γ_b and the crack-face Γ_{c^+} are discretized using straight elements.

The time t is divided into K equidistant time-steps.

The boundary variables and the generalized CODs are approximated by the interpolation functions as shown next for displacements:

$$u_I(\mathbf{y},\tau)=\sum_{k=1}^{K}\sum_{e=1}^{E_b}\sum_{\alpha=1}^{N}\psi_\alpha^e(\mathbf{y})\varphi^k(\tau)u_I^{e\alpha,k}, \tag{30}$$

where $\psi_\alpha^e(\mathbf{y})$ and $\varphi^k(\tau)$ are the spatial and the temporal shape functions, E_b is the number of elements of Γ_b and N is the number of nodes of each element.

For spatial discretization linear shape functions are adopted for elements away from crack-tips. For elements adjacent to the crack-tips "square-root" shape functions are implemented to describe the local behavior of the CODs properly. These shape functions allow an accurate and direct calculation of the dynamic field intensity factors from the numerically computed CODs.

The temporal discretization is performed using linear shape functions as following:

$$\begin{aligned}\varphi^k(\tau)=\frac{1}{\Delta t}\{&[\tau-(k-1)\Delta t]\mathrm{H}[\tau-(k-1)\Delta t]-2(\tau-k\Delta t)\mathrm{H}(\tau-k\Delta t)\\&+[\tau-(k+1)\Delta t]\mathrm{H}[\tau-(k+1)\Delta t]\}.\end{aligned} \tag{31}$$

The above described discretization scheme leads to the following system of linear algebraic equations

$$\mathbf{C}\mathbf{u}^K=\mathbf{U}^S\mathbf{t}^K-\mathbf{T}^S\mathbf{u}^K+\mathbf{T}^S\Delta\mathbf{u}^K+\sum_{k=1}^{K}[\mathbf{U}^{R;K-k+1}\mathbf{t}^k-\mathbf{T}^{R;K-k+1}\mathbf{u}^K+\mathbf{T}^{R;K-k+1}\Delta\mathbf{u}^K], \tag{32}$$

$$\mathbf{D}\mathbf{t}^K=\mathbf{V}^S\mathbf{t}^K-\mathbf{W}^S\mathbf{u}^K+\mathbf{W}^S\Delta\mathbf{u}^K+\sum_{k=1}^{K}[\mathbf{V}^{R;K-k+1}\mathbf{t}^k-\mathbf{W}^{R;K-k+1}\mathbf{u}^K+\mathbf{W}^{R;K-k+1}\Delta\mathbf{u}^K]. \tag{33}$$

In Eqs. (32) and (33), the superscripts S and R denote the corresponding matrices resulting from the static and the dynamic parts of the time-domain fundamental solutions.

According to Eqs. (20) and (21) the matrices arising in Eqs. (32) and (33) involve double integrals, which is common in the Galerkin-method due to the additional boundary integration. The second boundary integration reduces the strength of the strongly singular and the hypersingular kernels in the traction fundamental solutions, so that the intensity of the hypersingular integrals is comparable to the Cauchy principal value integrals in the collocation method [14,3]. Therefore the Galerkin-method allows the use of standard continuous elements for the spatial discretization of the boundary and the crack-faces, which reduces the number of the unknown boundary values in comparison to the discontinuous approximation in the collocation method [28,13]. Analytical techniques are used for a direct evaluation of the strongly singular and the hypersingular boundary integrals. The double integrations lead to different types of singularities. A review on different possibilities to compute the hypersingular integrals especially the singular double-integrals in the Galerkin-method has been presented by Gray [14]. Since linear temporal shape functions are used, all arising time integrations in the time-domain BIEs (20) and (21) can be performed analytically, which enhances the efficiency of the present time-domain BEM. Only the line-integrals over the unit-circle in the time-domain fundamental solutions have to be computed numerically, which can be done by standard Gaussian quadratures.

4.2. Time-stepping scheme

By using the causality and the time-translation properties of the time-domain fundamental solutions as well as the zero-initial conditions (8) and by invoking the boundary conditions (9), (10) and the crack-face boundary conditions (12) or (13), Eqs. (32) and (33) can be summarized and recast into the form

$$\mathbf{\Xi}^1\mathbf{x}^K=\mathbf{\Upsilon}^1\mathbf{y}^K+\sum_{k=1}^{K-1}(\mathbf{\Lambda}^{K-k+1}\mathbf{t}^k-\mathbf{\Theta}^{K-k+1}\mathbf{u}^k), \tag{34}$$

where $\mathbf{\Theta}^k$ and $\mathbf{\Lambda}^k$ are the system matrices, $\mathbf{u}^k$ is the vector containing the generalized displacements on external boundaries and the generalized CODs on crack-faces, $\mathbf{t}^k$ is the generalized traction vector, $\mathbf{\Xi}^1$ and $\mathbf{\Upsilon}^1$ are the rearranged system matrices and $\mathbf{x}^K$ and $\mathbf{y}^K$ are, respectively, the vectors containing the unknown and prescribed boundary data.

The computation of the unknown boundary data at the K-th time step as a function of the previous-ones is carried out following an explicit time-stepping scheme obtained from Eq. (34)

$$\mathbf{x}^K=(\mathbf{\Xi}^1)^{-1}\left[\mathbf{\Upsilon}^1\mathbf{y}^K+\sum_{k=1}^{K-1}(\mathbf{\Lambda}^{K-k+1}\mathbf{t}^k-\mathbf{\Theta}^{K-k+1}\mathbf{u}^k)\right]. \tag{35}$$

5. Computation of dynamic field intensity factors

The crack-tip fields for the generalized displacements (3) in a plane linear piezoelectric solid were derived by Pak [27] and Suo et al. [34]. Such fields show the well-known square-root behavior that, in this paper, is properly modeled by the implementation of square-root shape functions at the elements containing the crack-tip, as described in the previous section.

The dynamic field intensity factors (IFs) are directly evaluated from the computed generalized CODs at the interior node of the crack-tip element by an extrapolation method from

$$\begin{Bmatrix}K_{II}(t)\\K_I(t)\\K_{IV}(t)\end{Bmatrix}=\sqrt{\frac{2\pi}{l}}\mathbf{H}\begin{Bmatrix}\Delta u_1(l,t)\\\Delta u_2(l,t)\\\Delta\phi(l,t)\end{Bmatrix}, \tag{36}$$

where l is the length of the crack-tip element; K_I and K_{II} are the mode-I and mode-II stress intensity factors, respectively; K_{IV} is the electric displacement intensity factor; and the matrix $\mathbf{H}$ is defined by

$$\mathbf{H}=[\mathrm{Re}(i\mathbf{G}\mathbf{J}^{-1})]^{-1}, \tag{37}$$

where the tensors $\mathbf{G}$ and $\mathbf{J}$, depending on the materials properties, can be computed from the following eigenvalue equation:

$$\left(\begin{array}{c|c}-\mathbf{L}^{-1}\mathbf{M} & -\mathbf{L}^{-1}\\ \hline \mathbf{N}-\mathbf{M}^T\mathbf{L}^{-1}\mathbf{M} & -\mathbf{M}^T\mathbf{L}^{-1}\end{array}\right)\left(\begin{array}{c}\mathbf{G}_m\\ \hline \mathbf{J}_m\end{array}\right)=\eta_m\left(\begin{array}{c}\mathbf{G}_m\\ \hline \mathbf{J}_m\end{array}\right)\quad(\text{no sum on m}), \tag{38}$$

with $\mathbf{L}$, $\mathbf{M}$ and $\mathbf{N}$ being the tensors defined in (A.18).

6. Numerical examples

In the following, numerical examples are presented to show the accuracy and the efficiency of the developed time-domain

BEM. For the sake of clarity, the following contraction index notation will be used for the elastic stiffness and piezoelectric tensors

$$C_{ijkl} \to C_{\alpha\beta}; \quad e_{lij} \to e_{l\alpha}, \tag{39}$$

where

$$\alpha = \begin{cases} i & \text{if } i=j, \\ 9-(i+j) & \text{if } i\neq j, \end{cases} \quad \beta = \begin{cases} k & \text{if } k=l, \\ 9-(k+l) & \text{if } k\neq l. \end{cases} \tag{40}$$

To indicate the ratio between the mechanical and the electrical impacts, the following parameter is introduced

$$\kappa = \frac{e_{22}}{\varepsilon_{22}}\frac{D_0}{\sigma_0}, \tag{41}$$

where σ_0 and D_0 are the loading amplitudes.

In all the examples, the dynamic mode-I and mode-II stress intensity factors and the dynamic mode-IV electrical displacement intensity factor are normalized by

$$K_I^*(t) = \frac{K_I(t)}{K_I^{st}}, \quad K_{II}^*(t) = \frac{K_{II}(t)}{K_I^{st}}, \quad K_{IV}^*(t) = \frac{e_{22}}{\varepsilon_{22}}\frac{K_{IV}(t)}{K_I^{st}}, \tag{42}$$

with $K_I^{st} = f\sigma_0\sqrt{\pi a}$, where $f=1$ when mechanical loading is applied and $f=\kappa$ for the case of pure electrical loading; and a is the half-length of an internal crack or the length of an edge crack, as detailed in the geometry of each example.

To ensure the stability of the explicit time-stepping scheme, the spatial size of the elements and the time-step cannot be chosen independently [8,16]. As for homogeneous, isotropic and linear elastic solids, the following relation is used in the present time-domain BEM

$$\lambda = \frac{c_{max}\Delta t}{l_e}, \tag{43}$$

where l_e represents the element-length and c_{max} denotes the larger one of the velocities of the quasi-longitudinal and quasi-transverse waves

$$c_L = \sqrt{C_{22}/\rho}, \quad c_T = \sqrt{C_{66}/\rho}. \tag{44}$$

It has been reported in [8] that good results can be obtained by using $\lambda \approx 1$. Anyway the spatial Galerkin-method improves the stability of the explicit time-stepping scheme significantly while the computational time is comparable with the collocation method [16,36]. Numerical investigations of cracked anisotropic solids subjected to impact loadings confirm a stable time-stepping scheme for $\lambda \geq 0.6$ [36]. The following examples are computed using a time-step range of $0.7 \leq \lambda \leq 2$.

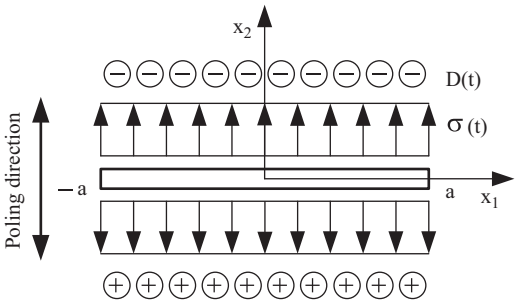

Fig. 2. A finite crack in an infinite linear piezoelectric solid subjected to an impact loading.

6.1. A finite crack in an infinite plate

In the first example, we consider a finite crack of length $2a$ in an infinite linear piezoelectric solid (Fig. 2) subjected to an impact tensile loading $\sigma(t) = \sigma_0 H(t)$ and an impact electrical loading $D(t) = D_0 H(t)$, where σ_0 and D_0 are the loading amplitudes and $H(t)$ is the Heaviside step function.

The crack is discretized into 20 elements and a normalized time-step of $c_L\Delta t/a = 0.05$ is chosen. Plain strain condition is assumed and Barium Titanate ($BaTiO_3$) is considered in the numerical calculations, which has a mass density of $\rho = 5800\,\mathrm{kg/m^3}$ and the following material constants

$$C_{11} = 150.0\,\mathrm{GPa}, \quad C_{12} = 146.0\,\mathrm{GPa}, \quad C_{22} = 44.0\,\mathrm{GPa}, \quad C_{66} = 66.0\,\mathrm{GPa},$$

$$e_{21} = -4.35\,\mathrm{C/m^2}, \quad e_{22} = 17.5\,\mathrm{C/m^2}, \quad e_{16} = 11.4\,\mathrm{C/m^2},$$

$$\varepsilon_{11} = 9.87\,\mathrm{C/(GV\,m)}, \quad \varepsilon_{22} = 11.2\,\mathrm{C/(GV\,m)}. \tag{45}$$

A comparison of the normalized dynamic intensity factors obtained by the present time-domain BEM using impermeable electric crack-face boundary conditions (12) with those of García-Sánchez et al. [11] for combined mechanical and electrical loadings is presented in Fig. 3. Benchmark results by Shindo et al. [29] for pure mechanical impact are included in Fig. 3. The normalized dynamic mode-I and mode-IV IFs of the present TDBEM are in good agreement with the reference results for all considered loadings. Only a small deviation in the arising time

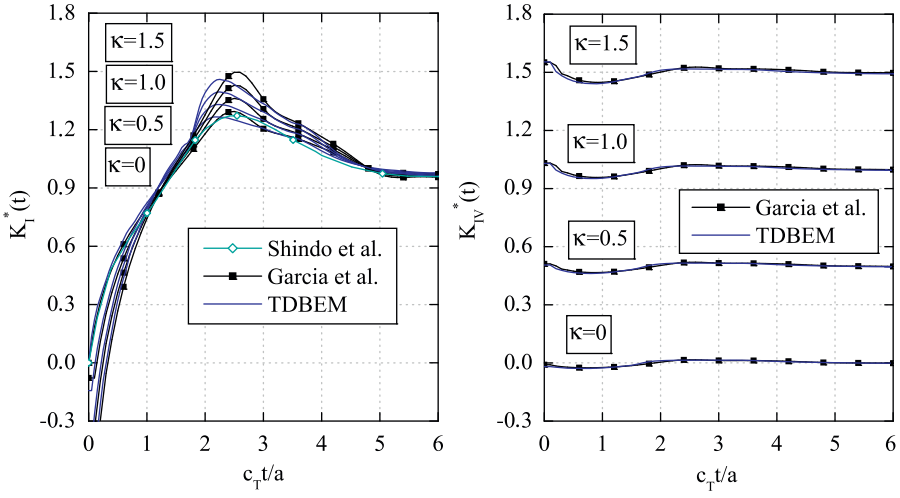

Fig. 3. Normalized dynamic IFs for $\kappa = 0$, 0.5, 1 and 1.5.

of the maximum mode-I IF is observed for all κ−values. The dynamic mode-II IF vanishes, since no shear stress components are induced for the applied tensile loading in the case of a transversely isotropic material behavior. As shown in Fig. 3, the variation of the loading parameter κ has a clear influence on the normalized dynamic mode-I and mode-IV IFs. The variation of the mode-I IF with time is similar to that previously observed for isotropic solids. It increases until reaching the maximum values and then decreases to attain their corresponding static values in the large-time limit. The dynamic overshoot of the mode-I IF increases or decreases with the intensity of the electrical impact. In contrast, the mode-IV IF is only weakly dependent on the time, which is a consequence of quasi-electrostatic assumption of the electrical field. However, it shows a stronger dependence on the load parameter value κ.

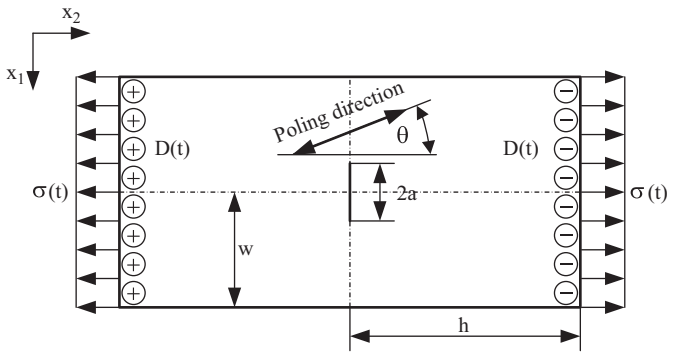

Fig. 4. A rectangular plate with a central crack under impact loading.

6.2. A central crack in a rectangular plate

In the next example let us consider a homogeneous and linear piezoelectric rectangular plate with a central crack of length 2a as shown in Fig. 4. The cracked plate is subjected to an impact tensile loading $\sigma(t)=\sigma_0 H(t)$ and an impact electrical loading $D(t)=D_0 H(t)$.

In the numerical calculations the geometrical data $h=20.0$ mm, $2w=h$ and $2a=4.8$ mm are assumed and Zirconate Titanate (PZT-5H) is investigated, which has a mass density of $\rho=7500\,\mathrm{kg/m^3}$ and the following material properties

$$C_{11}=126.0\,\mathrm{GPa},\quad C_{12}=84.1\,\mathrm{GPa},\quad C_{22}=117.0\,\mathrm{GPa},$$
$$C_{66}=23.0\,\mathrm{GPa},$$
$$e_{21}=-6.5\,\mathrm{C/m^2},\quad e_{22}=23.3\,\mathrm{C/m^2},\quad e_{16}=17.0\,\mathrm{C/m^2},$$
$$\varepsilon_{11}=15.04\,\mathrm{C/(GV\,m)},\quad \varepsilon_{22}=13.0\,\mathrm{C/(GV\,m)}, \tag{46}$$

where the poling direction of the material coincides with the axis x_2 normal to the crack line ($\theta=0$ in Fig. 4, θ being the angle between the x_2−axis and the poling direction of the material).

The external boundary is discretized into a uniform mesh with an element-length of 1.0 mm to totalize 120 linear boundary elements and the crack is divided into 12 elements. A normalized time-step of $c_L\Delta t/h=0.04$ is chosen and plane strain condition is assumed.

Numerical results obtained by the present time-domain BEM are compared in Fig. 5 with those obtained using the commercial FEM program ANSYS for different loading cases κ and impermeable electrical crack-faces for $\theta=0^\circ$. Only FEM results for $\kappa=0.5$ and $\kappa=1.0$ are included for the sake of clarity. In the

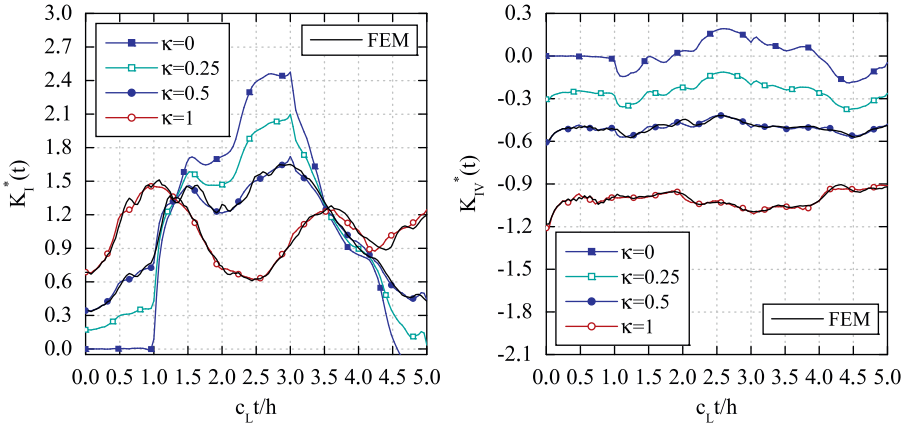

Fig. 5. Normalized dynamic IFs for $\kappa=0$, 0.25, 0.5 and 1.

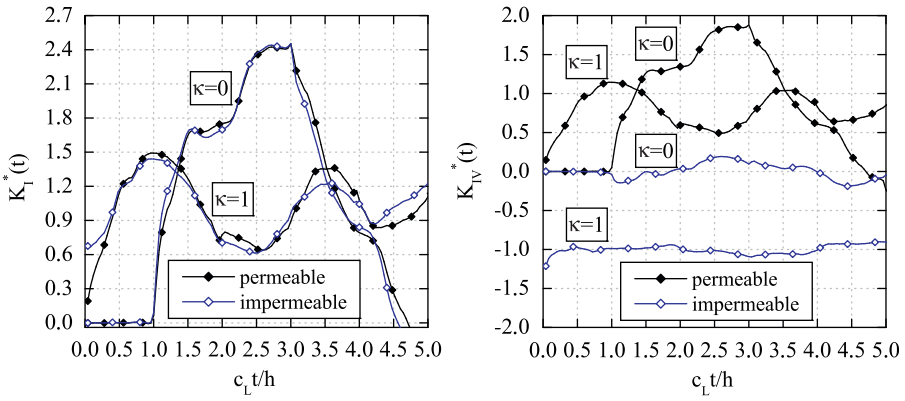

Fig. 6. Effects of different electrical crack-face conditions on the normalized dynamic IFs.

FE calculations the element type PLANE223 is chosen and quarter-point elements are implemented to describe the local behavior of the CODs at crack-tips properly. The dynamic IFs are computed directly by the CODs. The FE mesh used consists of 4459 elements. Normalized dynamic mode-I and mode-IV IFs are in good agreement for all considered loadings. The dynamic mode-II IF vanishes, since no shear stress components are induced in the case of a transversely isotropic material behavior. The peak values of the normalized dynamic IFs decrease with increasing electrical loading. It can be observed that, when applying an electrical impact, i.e. $\kappa \neq 0$, the normalized dynamic mode-I IF starts from a non-zero value at $t = 0$. This value is proportional to the electrical impact. This is due to the quasi-electrostatic assumption on the electrical field, which implies that the cracked plate is immediately subjected to an electrical impact and therefore the crack opens at $t = 0$. In contrast, the elastic waves induced by the mechanical impact need some time to reach and excite the crack, as clearly observed for the $\kappa = 0$ case.

To illustrate the effects of the different electrical crack-face conditions, given in Eqs. (12) and (13), on the dynamic IFs several computations have been carried out. The numerical results of the present time-domain BEM for $\kappa = 0$ and 1 are presented in Fig. 6. The values of the normalized dynamic mode-I IF induced by a pure mechanical and a combined mechanical/electrical impact loading are very similar without a significant difference between the impermeable and the permeable electrical crack-face conditions. In contrast, the values obtained for the normalized dynamic mode-IV IF are very different for the impermeable and the permeable cracks. This is due to the fact that the impermeable crack shields the electric induction, while the permeable crack does not induce such shielding.

Next, the influence of the orientation of the material poling direction with respect to the axis x_2 on the IFs is investigated. The comparison of the normalized dynamic IFs for different rotation angles $\theta = 0^\circ$, 30°, 60° and 90° is presented in Fig. 7. To point out the influence of the scattered wave fields on the dynamic results, the corresponding static IFs are additionally presented in Table 1.

The computed results are compared in Fig. 7 with those obtained using the FEM code ANSYS. Only FEM results for $\theta = 60^\circ$ and $\theta = 90^\circ$ have been included for the sake of clarity. Good agreement between both sets of results is observed for all the cases.

A variation of the angle θ leads to different poling direction referring to the crack-faces, which results in decreasing electrical IFs for increasing angles θ. In the case of $\theta = 90^\circ$ the electrical intensity factor is zero since the piezoelectric effect vanishes for a crack-face tangential to the poling direction. In contrast to the static loading case, the dynamic mode-I and mode-II IFs show a significant dependence on the angle θ, which is induced by the scattered wave fields.

Table 1
Normalized static intensity factors for different rotation angles θ.

θ (deg)	K_I^*	K_{II}^*	K_{IV}^*
0	1.05	0.00	−1.03
30	1.05	0.00	−0.90
60	1.05	0.00	−0.53
90	1.05	0.00	0.00

6.3. A rectangular plate with a pair of interacting collinear cracks

In the following example a pair of interacting collinear cracks in a homogenous, linear piezoelectric rectangular plate subjected to an impact tensile loading $\sigma(t) = \sigma_0 \mathrm{H}(t)$ and an impact electrical loading $D(t) = D_0 \mathrm{H}(t)$ on the upper and lower boundary is investigated.

The geometry of the problem is shown in Fig. 8, with the following geometrical data: $h = 16.0$, $w = 20.0$, $d = 12.0$ and

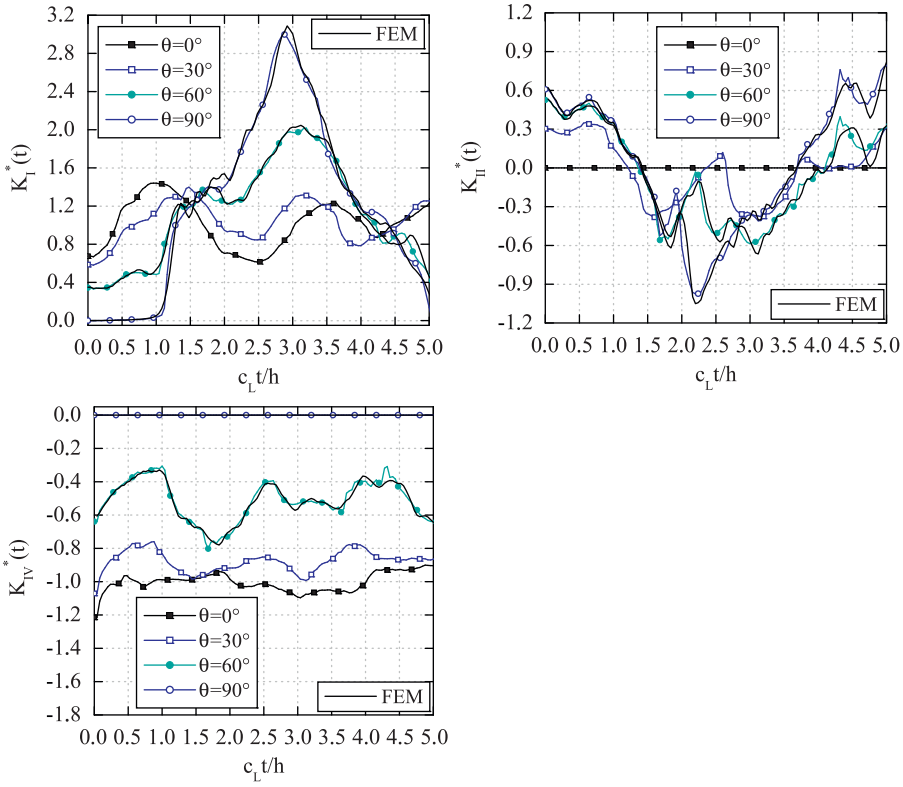

Fig. 7. Comparison of the normalized dynamic IFs for different rotation angles θ.

$2a = 4.0$ mm. The material is a Barium Titanate with the material constants given in Eq. (45). The spatial discretization of the external boundary of the plate corresponds to a uniform mesh with 144 elements, while both cracks are divided into 15 elements. A time-step $c_L \Delta t/h = 0.04$ and plane strain condition are assumed in the numerical calculations.

The corresponding numerical results are presented in Fig. 9 for different loadings. Only one of the tips (tip B) is taken into consideration for the sake of brevity. Once more, the normalized mode-I and mode-IV dynamic intensity factors obtained by the present time-domain BEM agree well with the FEM results using ANSYS. Only FEM results for pure mechanical and pure electrical loading are included for the sake of clarity. The FE mesh used consists of 9691 elements. Since no shear stress components are induced and the material investigated is transversely isotropic, the mode-II IF vanishes for all the considered loadings. The global behavior observed in the different curves is similar for the applied loadings, with just a significant change in the peak values. As in the previous examples, the dynamic mode-I IF induced by the pure mechanical impact loading ($\kappa = 0$) is zero until the elastic waves arrive at the crack-tips near $c_L t/h = 0.5$. After this instant, the curves increase rapidly. However, the normalized dynamic IFs induced by an electrical loading start from a non-zero value due to the quasi-electrostatic assumption and, as in the case of a pure mechanical loading, they increase rapidly after $c_L t/h = 0.5$. Since the geometry of the cracked plate and the external loading are symmetric with respect to the vertical midline, the dynamic IFs of both cracks are identically.

6.4. A rectangular plate with a pair of interacting edge cracks

In the last example, a homogeneous and linear piezoelectric rectangular plate with a pair of interacting edge cracks is considered. As depicted in Fig. 10 the cracked plate is subjected to an impact tensile loading $\sigma(t) = \sigma_0 \mathrm{H}(t)$ in the normal direction to the crack-faces and an impact electrical loading $D(t) = D_0 \mathrm{H}(t)$.

The cracked plate has the geometrical data $h = 20.0$, $w = 15.0$ and $a = 5.0$ mm. Two different crack separations are considered in order to illustrate the crack interactions, with values $d = 0.0$ and 10.0 mm. The material is the same PZT-5H considered above but with the poling direction rotated by an angle $\theta = 45^\circ$ with respect to the x_2-axis, which is normal to both cracks. The external boundary is divided into a uniform mesh with 70 elements, while both cracks are discretized by 20 elements. A normalized time-step $c_L \Delta t/h = 0.08$ is chosen in the numerical calculations. Plane strain condition is assumed.

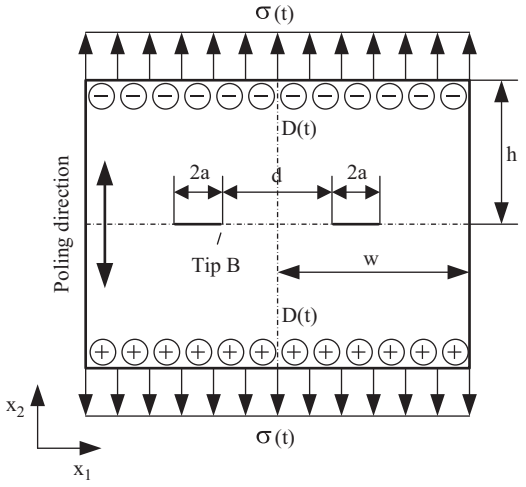

Fig. 8. A rectangular plate with a pair of interacting cracks.

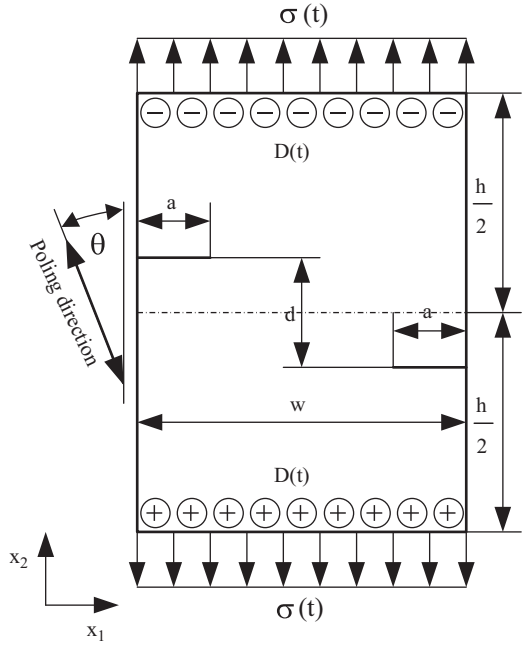

Fig. 10. A rectangular plate with a pair of interacting edge cracks.

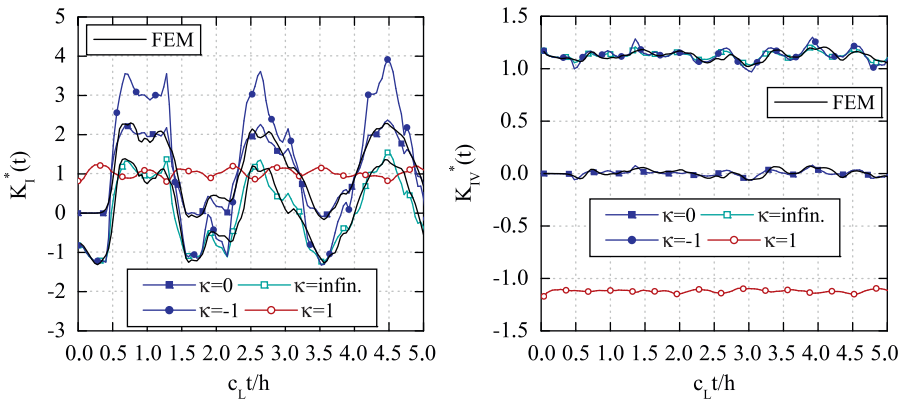

Fig. 9. Normalized dynamic IFs for Tip B.

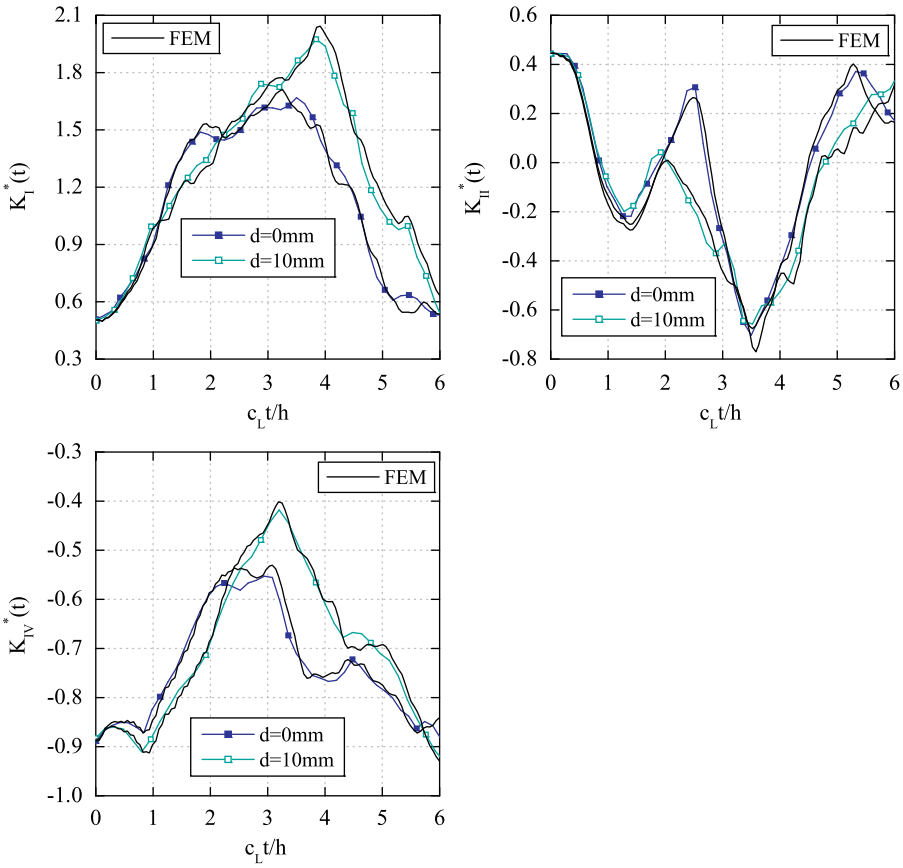

Fig. 11. Normalized dynamic IFs for different distances d between both edge cracks.

The corresponding numerical results under impermeable electrical crack-face condition and a loading parameter $\kappa = 1$ are shown in Fig. 11. Due to the geometry of the cracked plate and the external loading, the dynamic IFs obtained at both crack-tips are identical. The normalized dynamic IFs obtained by the present time-domain boundary element method (TDBEM) show a good agreement with the FEM results using ANSYS with a FE mesh consisting of 8759 elements. Some small deviations are observed for both distances d. The global behavior of the normalized dynamic mode-I IFs is similar for both considered distances d. Since an electrical impact is applied the normalized mode-I dynamic IFs start from a non-zero value. In comparison to the results for two central collinear cracks in a rectangular plate, shown in Fig. 9, the normalized dynamic mode-II and mode-IV IFs show a more complex behavior, which is presumably induced by the rotation of the material axis with $\theta = 45^{\circ}$ to the crack-faces.

7. Conclusions

This paper presents a time-domain BEM for 2D transient dynamic crack analysis in homogenous, anisotropic and linear piezoelectric solids.

On the external boundary of the cracked solid the classical displacement BIEs are applied, while on the crack-faces the hypersingular traction BIEs are used. The dynamic time-domain fundamental solutions for homogenous, anisotropic and linear piezoelectric solids derived by Wang and Zhang [35] are implemented in the present time-domain BEM. The spatial discretization is performed by a Galerkin-method with linear elements and square-root crack-tip elements adjacent to the crack-tips. The use of crack-tip elements ensures a direct and an accurate calculation of the dynamic intensity factors from the numerically computed generalized crack-opening-displacements. A collocation method with linear shape function is applied for the temporal discretization. With the exception of the line integrals over a unit circle arising in the time-domain fundamental solutions, the temporal and the spatial integrations are computed analytically which makes the present time-domain BEM particularly attractive. Due to this special feature, the present Galerkin-BEM is computationally comparable to the widely used collocation method, although the Galerkin-method involves double integrals rather than the single integrals appearing in the collocation method. Analytical integration of the boundary integrals is only possible for straight elements, while numerical integrations would be necessary for higher order curved elements, with the corresponding increase in the computational cost. The present time-domain BEM is general and has no limitations on the material anisotropy, the configuration of the cracks and the dynamic loading conditions. Numerical examples are presented and discussed to verify the accuracy and the efficiency of the present time-domain BEM for transient dynamic crack analysis in 2D infinite and finite piezoelectric solids. The effects of the combined application of electrical and mechanical impact loadings, different electrical crack-face conditions and the poling direction on the dynamic intensity factors are investigated. Comparisons of the present numerical results with those obtained by other methods show a good agreement.

Acknowledgments

This work was supported by the Ministerio de Ciencia e Innovación of Spain and the Consejería de Innovación, Ciencia y

Empresa of Andalucía (Spain) under Projects DPI2007-66792-C02-02 and P06-TEP-02355, and the German Research Foundation (DFG, Project no. ZH 15/6-1 and ZH 15/6-3). The financial support is gratefully acknowledged.

Appendix A

A.1. Regular part of the time-domain fundamental solutions

The regular (dynamic) part of displacements fundamental solution in Eq. (23) can, unfortunately, not be expressed in a closed-form. For the 2D case it is given by the following line integral over a unit circle:

$$u_{IJ}^R(\mathbf{x},\mathbf{y},t)=\frac{\mathrm{H}(t)}{4\pi^2}\int_{|\mathbf{n}|=1}\sum_{m=1}^{3}\frac{P_{IJ}^m}{\rho c_m^2}\log|c_m t+\mathbf{n}(\mathbf{y}-\mathbf{x})|\,\mathrm{d}\mathbf{n}. \tag{A.1}$$

The term $P_{IJ}^m(\mathbf{n})$ present in (A.1) is the so-called projection operator and c_m are the phase velocity of the waves.

The projector operator can be obtained as following:

$$P_{IJ}^m(\mathbf{n})=\begin{cases}\dfrac{E_{ij}^m(\mathbf{n})}{E_{kk}^m(\mathbf{n})}, & I,J=1,2,\\ -\dfrac{E_{iq}^m(\mathbf{n})\Gamma_{q4}(\mathbf{n})}{\Gamma_{44}(\mathbf{n})E_{kk}^m(\mathbf{n})}, & I=1,2;\ J=4,\\ \dfrac{\Gamma_{4p}(\mathbf{n})E_{pq}^m(\mathbf{n})\Gamma_{q4}(\mathbf{n})}{\Gamma_{44}^2(\mathbf{n})E_{kk}^m(\mathbf{n})}, & I=J=4,\end{cases} \tag{A.2}$$

where

$$\Gamma_{IJ}(\mathbf{n})=C_{kIJl}n_k n_l \tag{A.3}$$

and

$$E_{ij}^m(\mathbf{n})=\mathrm{adj}[Z_{ij}(\mathbf{n})-\rho c_m^2\delta_{ij}], \tag{A.4}$$

with

$$Z_{ij}(\mathbf{n})=\Gamma_{ij}(\mathbf{n})-\frac{\Gamma_{i4}(\mathbf{n})\Gamma_{4j}(\mathbf{n})}{\Gamma_{44}(\mathbf{n})}. \tag{A.5}$$

Regarding the phase velocities, they are computed from the following eigenvalues equation

$$\det[Z_{ij}(\mathbf{n})-\rho c_m^2\delta_{ij}]=0. \tag{A.6}$$

Similarly to the displacements, the regular dynamic parts of the tractions and the higher-order traction fundamental solutions can be expressed as

$$t_{IJ}^R(\mathbf{x},\mathbf{y},t)=\frac{\mathrm{H}(t)}{4\pi^2}\int_{|\mathbf{n}|=1}\sum_{m=1}^{3}\frac{Q_{IJ}^m}{\rho c_m^2}\log|c_m t+\mathbf{n}(\mathbf{y}-\mathbf{x})|\,\mathrm{d}\mathbf{n}, \tag{A.7}$$

$$v_{IJ}^R(\mathbf{x},\mathbf{y},t)=-\frac{\mathrm{H}(t)}{4\pi^2}\int_{|\mathbf{n}|=1}\sum_{m=1}^{3}\frac{R_{IJ}^m}{\rho c_m^2}\log|c_m t+\mathbf{n}(\mathbf{y}-\mathbf{x})|\,\mathrm{d}\mathbf{n}, \tag{A.8}$$

$$w_{IJ}^R(\mathbf{x},\mathbf{y},t)=-\frac{\mathrm{H}(t)}{4\pi^2}\int_{|\mathbf{n}|=1}\sum_{m=1}^{3}\frac{S_{IJ}^m}{\rho c_m^2}\frac{1}{c_m t+\mathbf{n}(\mathbf{y}-\mathbf{x})}\,\mathrm{d}\mathbf{n}, \tag{A.9}$$

where

$$Q_{IJ}^m(\mathbf{n},\mathbf{e})=C_{qIKr}e_q(\mathbf{y})n_r P_{KJ}^m(\mathbf{n}), \tag{A.10}$$

$$R_{IJ}^m(\mathbf{n},\mathbf{e})=C_{pIKs}e_p(\mathbf{x})n_s P_{KJ}^m(\mathbf{n}), \tag{A.11}$$

$$S_{IJ}^m(\mathbf{n},\mathbf{e})=C_{pIKs}e_p(\mathbf{x})n_s(\mathbf{x})C_{qJLr}e_q(\mathbf{y})n_r(\mathbf{y})P_{KL}^m(\mathbf{n}). \tag{A.12}$$

It should be remarked that the dynamic parts of the time-domain fundamental solutions are regular except on the wave front $c_m t+\mathbf{n}\cdot(\mathbf{y}-\mathbf{x})=0$.

A.2. Singular part of the time-domain fundamental solutions

The singular part of the time-domain fundamental solutions (23) corresponds to the static fundamental solutions for homogeneous, anisotropic and linear piezoelectric solids, which can be given in explicit form as [6,35]

$$u_{IJ}^S(\mathbf{x},\mathbf{y})=\frac{1}{\pi}\mathrm{Im}\sum_{m=1}^{3}\frac{A_{IJ}(\eta_m)}{\partial_\eta D(\eta_m)}\log[\mathbf{d}_m(\mathbf{y}-\mathbf{x})]+F_{IJ}, \tag{A.13}$$

with

$$A_{IJ}(\eta)=\mathrm{adj}[\Gamma_{IJ}(1,\eta)],\ \mathbf{d}=(1,\eta), \tag{A.14}$$

$$D(\eta)=\det[\Gamma_{IJ}(1,\eta)]. \tag{A.15}$$

In Eqs. (A.13)–(A.15), $D(\eta)$ is a polynomial of sixth order with real-valued coefficients. It has three complex roots η_m and three complex conjugates of η_m, which are determined by the following characteristic equation

$$D(\eta_m)=0. \tag{A.16}$$

In Eqs. (A.14) and (A.15) $\Gamma_{IJ}(1,\eta)$ is defined by

$$\Gamma_{IJ}(1,\eta)=L_{IJ}\eta^2+(M_{IJ}+M_{IJ}^T)\eta+N_{IJ}, \tag{A.17}$$

with

$$L_{IJ}=C_{2IJ2},\quad M_{IJ}=C_{2IJ1},\quad N_{IJ}=C_{1IJ1}. \tag{A.18}$$

The constant terms F_{IJ} in the displacement fundamental solutions $u_{IJ}^S(\mathbf{x},\mathbf{y})$ are inessential for static problems, but they are required for the dynamic time-domain BEM [6,35]

$$F_{IJ}=-\frac{1}{\pi}\mathrm{Im}\sum_{m=1}^{3}\frac{A_{IJ}(\eta_m)}{\partial_\eta D(\eta_m)}\log[\eta_m+\mathrm{i}]. \tag{A.19}$$

Substitution of the displacement fundamental solutions (A.13) into Eqs. (16), (18) and (19) yields the following explicit expressions for the singular static parts of the traction and the higher order traction fundamental solutions

$$t_{IJ}^S(\mathbf{x},\mathbf{y})=\frac{1}{\pi}\mathrm{Im}\sum_{m=1}^{3}\frac{B_{IJ}(\eta_m)}{\partial_\eta D(\eta_m)}\frac{\mathbf{d}_m\cdot\mathbf{e}(\mathbf{y})}{\mathbf{d}_m\cdot(\mathbf{y}-\mathbf{x})}, \tag{A.20}$$

$$v_{IJ}^S(\mathbf{x},\mathbf{y})=-\frac{1}{\pi}\mathrm{Im}\sum_{m=1}^{3}\frac{B_{IJ}(\eta_m)}{\partial_\eta D(\eta_m)}\frac{\mathbf{d}_m\cdot\mathbf{e}(\mathbf{x})}{\mathbf{d}_m\cdot(\mathbf{y}-\mathbf{x})}, \tag{A.21}$$

$$w_{IJ}^S(\mathbf{x},\mathbf{y})=-\frac{1}{\pi}\mathrm{Im}\sum_{m=1}^{3}\frac{C_{IJ}(\eta_m)}{\partial_\eta D(\eta_m)}\frac{\mathbf{d}_m\cdot\mathbf{e}(\mathbf{x})\,\mathbf{d}_m\cdot\mathbf{e}(\mathbf{y})}{[\mathbf{d}_m\cdot(\mathbf{y}-\mathbf{x})]^2}, \tag{A.22}$$

where

$$B_{IJ}(\eta_m)=(L_{IP}\eta_m+M_{IP})A_{PJ}(\eta_m), \tag{A.23}$$

$$C_{IJ}(\eta_m)=(L_{IP}\eta_m+M_{IP})A_{PK}(\eta_m)(L_{JK}\eta_m+M_{JK}). \tag{A.24}$$

From the above Eqs. (A.13), (A.20)–(A.22) it follows that the static displacement fundamental solutions have a weak logarithmic singularity $\log|\mathbf{y}-\mathbf{x}|$, the static traction fundamental solutions have a strong singularity $1/|\mathbf{y}-\mathbf{x}|$, and the higher order static traction fundamental solutions have a hypersingularity $1/|\mathbf{y}-\mathbf{x}|^2$ at $\mathbf{y}=\mathbf{x}$, which require special attention in the numerical implementation of the time-domain BEM.

References

[1] Aliabadi MH. The boundary element method volume 2, applications in solids and structures. New York: Computational Mechanics Publications, Wiley; 2002.

[2] Barnett DM, Lothe J. Dislocations and line charges in anisotropic piezoelectric insulators. Physica Status Solidi (b) 1975;76:105–11.

[3] Bonnet M, Guiggiani M. Direct evaluation of double singular integrals and new free terms in 2D (symmetric) Galerkin BEM. Computer Methods in Applied Mechanics and Engineering 2003;192:2565–96.

[4] Daros H, Antes H. Dynamic fundamental solutions for transversely isotropic piezoelectric materials of crystal class 6 mm. International Journal of Solids and Structures 2000;37:1639–58.

[5] Daros H. A fundamental solutions for transversely isotropic, piezoelectric solids under electrically irrotational approximation. Mechanics Research Communications 2002;29:61–71.

[6] Denda M, Araki Y, Yong YK. Time-harmonic BEM for 2-D piezoelectricity applied to eigenvalue problems. International Journal of Solids and Structures 2004;41:7241–65.

[7] Dziatkiewicz G, Fedelinski P. Dynamic analysis of piezoelectric structures by the dual reciprocity boundary element method. In: Gatmiri B, Sellier A, Aliabadi MH, editors. Advances in boundary element techniques, vol. VII. UK: EC Ltd.; 2006. p. 121–6.

[8] Domínguez J. Boundary elements in dynamics. Southampton, UK: Computational Mechanics Publications; 1993.

[9] Enderlein M, Ricoeur A, Kuna M. Finite element techniques for dynamic crack analysis in piezoelectrics. International Journal of Fracture 2005;134:191–208.

[10] Enderlein M. Finite element method for dynamic crack analysis in piezoelectric structures under transient electro-mechanical loading. PhD thesis, TU Freiberg, Germany, 2007 [in German].

[11] García-Sánchez F, Zhang Ch, Sladek J, Sladek V. 2-D transient dynamic crack analysis in piezoelectric solids by BEM. Computational Material Science 2007;39:179–86.

[12] García-Sánchez F, Zhang Ch. A comparative study of three BEM for transient dynamic crack analysis of 2-D anisotropic solids. Computational Mechanics 2007;40:753–69.

[13] García-Sánchez F, Zhang Ch, Sáez A. 2-D transient dynamic analysis of cracked piezoelectric solids by a time domain BEM. Computer Methods in Applied Mechanics and Engineering 2008;197:3108–21.

[14] Gray LJ. Evaluation of singular and hypersingular Galerkin boundary integrals: direct limits and symbolic computation. In: Sladek V, Sladek J, editors. Advances in boundary elements Southampton, UK: Computational Mechanics Publishers; 1998. p. 33–84.

[15] Gross D, Dineva P, Rangelov T. BIEM solution of piezoelectric cracked finite solids under time-harmonic loading. Engineering Analysis with Boundary Elements 2007;31:152–62.

[16] Guoyou Y, Mansur WJ, Carrer JAM, Gong L. Stability of Galerkin and collocation time-domain boundary element method as applied to the scalar wave equation. Computers and Structures 2000;74:495–506.

[17] Hong H-K, Chen JT. Derivations of integral equations of elasticity. Journal of Engineering Mechanics, ASCE 1988;114:1028–44.

[18] Chen JT, Hong H-K. Review of dual boundary element methods with emphasis on hypersingular integrals and divergent series. Applied Mechanics Reviews, ASME 1999;52(1):17–33.

[19] Kögl M, Gaul L. A boundary element method for transient piezoelectric analysis. Engineering Analysis with Boundary Elements 2000;24:591–8.

[20] Khutoryansky N, Sosa H. Dynamic representation formulas and fundamental solutions for piezoelectricity. International Journal of Solids and Structures 1995;32:3307–25.

[21] Khutoryansky NM, Sosa H. Construction of dynamic fundamental solutions for piezoelectric solids. Applied Mechanics Reviews 1995;48:222–229.

[22] Kuna M. Fracture mechanics of piezoelectric materials—where are we right now? Engineering Fracture Mechanics 2009; in press, DOI:10.1016/j.engfracmech.2009.03.016.

[23] Liu GR, Dai KY, Lim KM, Gu YT. A point interpolation mesh free method for static and frequency analysis of two-dimensional piezoelectric structures. Computational Mechanics 2000;29:510–9.

[24] Lubich C. Convolution quadrature and discretized operational calculus I. Numerische Mathematik 1988;52:129–45.

[25] Lubich C. Convolution quadrature and discretized operational calculus II. Numerische Mathematik 1988;52:413–25.

[26] Norris N. Dynamic Green's functions in anisotropic piezoelectric thermoelastic and poroelastic solids. Proceedings of the Royal Society London Series A 1994;447:175–88.

[27] Pak YE. Linear electro-elastic fracture of piezoelectric materials. International Journal of Fracture 1992;54:79–100.

[28] Sáez A, García-Sánchez F, Domínguez J. Hypersingular BEM for dynamic fracture in 2-D piezoelectric solids. Computer Methods in Applied Mechanics and Engineering 2006;196:235–46.

[29] Shindo Y, Narita F, Ozawa E. Impact response of a finite crack in an orthotropic piezoelectric ceramic. Acta Mechanica 1999;137:99–107.

[30] Sirtori G, Maier G, Novati G, Miccoli S. A Galerkin symmetric boundary element method in elasticity: formulation and implementation. International Journal for Numerical Methods in Engineering 1992;35:255–82.

[31] Sladek J, Sladek V, Zhang Ch, García-Sánchez F, Wünsche M. Meshless Local Petrov–Galerkin method for plane piezoelectricity. Computer, Material and Continua 2006;4:109–18.

[32] Sladek J, Sladek V, Zhang Ch, Solek P, Starek L. Fracture analyses in continuously nonhomogeneous piezoelectric solids by the MLPG. Computer Modeling in Engineering and Sciences 2007;19:247–62.

[33] Sladek J, Sladek V, Zhang Ch, Solek P. Application of the MLPG to thermo-piezoelectricity. Computer Modeling in Engineering and Sciences 2007;22:217–233.

[34] Suo Z, Kuo C-M, Barnett DM, Willis JR. Fracture mechanics for piezoelectric ceramics. Journal of Mechanics and Physics of Solids 1992;4:739–765.

[35] Wang C-Y, Zhang Ch. 3-D and 2-D dynamic Green's functions and time-domain BIEs for piezoelectric solids. Engineering Analysis with Boundary Elements 2005;29:454–65.

[36] Wünsche M, Zhang Ch, García-Sánchez F, Sáez A, Sladek J, Sladek V. On two hypersingular time-domain BEM for dynamic crack analysis in 2D anisotropic elastic solids. Computer Methods in Applied Mechanics and Engineering 2009;198:2812–24.